ELSEVIER

Journal of Alloys and Compounds 408–412 (2006) 456–462

Journal of ALLOYS AND COMPOUNDS

www.elsevier.com/locate/jallcom

Hydrogen separation using proton-conducting perovskites

Hiroshige Matsumoto[a,*], Tetsuo Shimura[b], Hiroyasu Iwahara[b], Tohru Higuchi[c],
Keiji Yashiro[a], Atsushi Kaimai[a], Tatsuya Kawada[a], Junichiro Mizusaki[a]

[a] *Department of Applied Chemistry, Faculty of Engineering, Kyushu University, 6-10-1 Hakozaki, Higashi-ku, Fukuoka 812-8581, Japan*
[b] *Nagoya University, Furo-cho, Chikusa-ku, Nagoya 464-8603, Japan*
[c] *Department of Applied Physics, Tokyo University of Science, Tokyo 162-8601, Japan*
[d] *IMRAM, Tohoku University, Katahira, Aoba-ku, Sendai 980-8577, Japan*

Received 30 July 2004; received in revised form 24 November 2004; accepted 15 December 2004

Abstract

Two methods of hydrogen separation using proton-conducting perovskites, electrochemical hydrogen pumping with proton-conducting electrolytes and hydrogen sieving through protonic–electronic mixed conductors, are stated. In the former case, high temperature proton conductors (HTPCs) enable the hydrogen transport by external application of electricity. In the latter case, it is a fundamental concern how the protonic and electronic charge carriers coexist in oxides to allow hydrogen permeation. Experimental results and the problems for future investigations are discussed.

Keywords: Proton conductors; Hydrogen separation; Hydrogen pumps; Mixed conductors

---

1. Introduction

Ion-conducting solid materials are useful for energy conversion, gas separation, gas sensing and so on. Rare earth metals play an important role for the ionic conduction in the materials. Some perovskite-type oxides show protonic conduction at high temperatures [1–15]. Particularly, the choice of tetravalent cerium combined with an alkaline earth metal and a trivalent rare earth dopant, e.g., $SrCe_{0.95}Yb_{0.05}O_{3-\alpha}$, results in high protonic conductivity; various trivalent cations with different ionic radii are conveniently chosen from the lanthanoids to optimize the ion-conducting properties. Such a protonic conduction in solids can be useful for various applications, as instructively summarized by Iwahara [16] and Schober [17]. Namely, the proton conductors allow selective transport of hydrogen, and thus are most attractive in applying to hydrogen separation.

This paper deals with the following methods of hydrogen separation using proton-conducting perovskites, i.e., electrochemical hydrogen pumping with proton-conducting electrolytes and hydrogen sieving through protonic–electronic mixed conductors. General understanding of the proton-conducting perovskites is explained with the defect chemistry for the generation of protonic charge carriers. The two kinds of hydrogen separation are shown with experimental results and the problems to be solved are discussed from both practical and fundamental view points.

2. High temperature proton conductors

Some oxides, typically having perovskite-type structure with the general formula of ABO_3, show protonic conduction at high temperatures and are referred to as high temperature proton conductors (HTPCs) [1–17]. Either Ce or Zr is available as the B-site cation, i.e., cerates and zirconates can be chosen as HTPCs. In general, the cerates have high protonic

---

* Corresponding author. Tel.: +81 92 642 3552; fax: +81 92 642 3551.
E-mail address: matsumoto@cstf.kyushu-u.ac.jp (H. Matsumoto).

0925-8388/$ – see front matter
doi:10.1016/j.jallcom.2004.12.093

conductivity, while the zirconates are characterized by high chemical stability as well as good mechanical strength. Due to such a trade-off relation between the protonic conductivity and chemical/mechanical stability, we have to select the B-site element appropriately depending on the applications.

HTPCs are designed to have oxide ion vacancy by a partial substitution of trivalent cations for the B-site tetravalent ones. In a moist atmosphere, protons are formed in these oxides in accordance with the following defect equilibriums [3]:

$$V_O^{\bullet\bullet} + \tfrac{1}{2}O_2 \overset{K_1}{\rightleftarrows} O_O^{\times} + 2h^{\bullet} \quad (1)$$

$$H_2O + 2h^{\bullet} \overset{K_2}{\rightleftarrows} 2H^{\bullet} + \tfrac{1}{2}O_2 \quad (2)$$

$$H_2O + V_O^{\bullet\bullet} \overset{K_3}{\rightleftarrows} 2H^{\bullet} + O_O^{\times} \quad (3)$$

$$K_3 = K_1 K_2 \quad (4)$$

where $V_O^{\bullet\bullet}$, $O_O^{\times}$, $H^{\bullet}$ and $h^{\bullet}$ denote oxide ion vacancy, oxide ion at the regular site, proton and electron hole, expressed, respectively, in the Kröger–Vink notation, and K_n is the equilibrium constant.

Eq. (3) suggests that the incorporation of ambient water molecules into the oxide ion vacancies is essential for the generation of protons that are mobile in the oxide. Therefore, the HTPCs need ambient moisture; the oxygen partial pressure, $p(O_2)$, has only a little effect to the protonic conductivity. Since this equilibrium moves from the right hand side to the left as temperature increases, an oxide ionic conduction via oxide ion vacancies, $V_O^{\bullet\bullet}$, also arises with increasing temperature. The protonic and oxide-ionic transport numbers depend not only on the temperature but also on the materials and will be indicated individually for each HTPC present in the following sections.

One can find from Eq. (1) that the hole concentration increases with $p(O_2)$. Consequently, the HTPCs usually have a large hole conductivity in an oxidative atmosphere, like in air. The equilibrium goes to the left as $p(O_2)$ decreases, and the protonic conduction (with a contribution of oxide-ionic conduction) dominates in moist hydrogen. This feature allows the use of HTPCs as electrolytes for hydrogen pumps (Section 4). In the case of hydrogen-permeating membrane via protonic–electronic mixed conduction, the main subject is to manage a kind of electronic charge carriers surviving even in such reducing atmospheres (Section 5).

3. Experimental

Here, general experimental procedures and conditions for the following sections are given.

Proton-conducting specimens were prepared by the solid state reactions in the following manner. Powders of either carbonates (Ba and Sr) or oxides (Zr, Ru and rare earths) were used as starting materials. Their appropriately weighed amounts were mixed and calcined for 10 h in air typically at 1250 °C for cerates and at 1350 °C for zirconates. The products were ground with planetary ball mill, isostatically pressed in disk shape at 300 MPa, and sintered for 10 h in air to obtain dense ceramics; typical sintering temperatures were 1550–1600 °C for strontium cerates, 1650 °C for barium cerates and 1650–1700 °C for strontium zirconates, respectively.

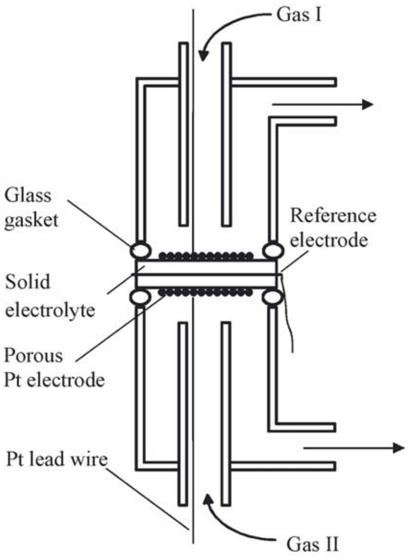

Fig. 1. Schematic structure of the electrochemical test cell.

Fig. 1 shows the schematic illustration of the electrochemical test cell. A disk specimen (0.5 mm thickness and 13–14 mm diameter), on which platinum paste was painted (projected area: 0.5 cm^2) as the anode and cathode, was placed between ceramic tubes with glass gaskets; the reference electrode was also prepared on the side of the electrolyte disk in the case of hydrogen-pumping experiments. Gases, usually hydrogen, argon or their mixtures, were introduced to the cell at given flow rates; the gases were moistened with water vapor typically at $p_W = 1.9 \times 10^3$ Pa. Hydrogen and water vapor in the outlet gases were determined by gas chromatography and with a chilled mirror hygrometer, respectively.

4. Hydrogen pumps

4.1. Principle and experimental procedure

The HTPCs can be used as the electrolytes for electrochemical hydrogen pumps as schematically shown in Fig. 2. When an electrochemical cell of a proton conductor is constructed and a direct current is sent to the cell, hydrogen in the anode compartment can be electrochemically pumped to the cathode, as shown in the figure, by the following electrode reactions:

$$H_2 \rightarrow 2H^+ + 2e^- \text{ (anode)} \quad (5)$$

$$2H^+ + 2e^- \rightarrow H_2 \text{ (cathode)} \quad (6)$$

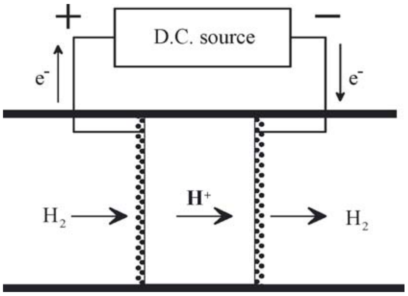

Fig. 2. Working principle of a hydrogen pump.

Experiments of hydrogen pumps were conducted with the following gas atmospheres:

$$\text{Moist } H_2,\ \text{Pt}|\text{electrolyte}|\text{Pt},\ \text{moist Ar} \tag{7}$$

The gases both in the anode and cathode compartments were moistened with water vapor because HTPCs need ambient water vapor to work. In addition, the water has a role to avoid too reducing atmosphere resulting in the occurrence of electronic conduction in the electrolyte as explained later. In order to evaluate the energy efficiency of the hydrogen pumps, electrode overpotentials were evaluated as follows. The electric potentials of the anode and cathode against the reference electrode, $V_{RA}(j)$ and $V_{RC}(j)$, were measured as functions of the current density, j. The overpotentials, defined as the changes in the potentials from those under open circuit condition, consist of electrode reaction polarization, η_{RA} and η_{RC} (the second subscript means either anode or cathode), overpotentials due to the changes in hydrogen concentrations, η_{CA} and η_{CC}, and ohmic losses, η_{OA} and η_{OC}, as written in Eqs. (8) and (9).

$$V_{RA}(j) - V_{RA}(0) = \eta_{RA} + \eta_{CA} + \eta_{OA} \tag{8}$$

$$V_{RC}(j) - V_{RC}(0) = -(\eta_{RC} + \eta_{CC} + \eta_{OC}) \tag{9}$$

The ohmic loss and the changes in the hydrogen pressure can be evaluated by the current interrupt method and gas chromatography, respectively, to obtain the rest reaction polarization, which directly leads to the energy dissipation at the electrodes.

4.2. Hydrogen-pumping performance of a cerate and a zirconate

Fig. 3 compares hydrogen-pumping characteristics when a cerate and a zirconate are used as the proton-conducting electrolytes. $SrCe_{0.95}Yb_{0.05}O_{3-\alpha}$ [18] and $SrZr_{0.9}Y_{0.1}O_{3-\alpha}$ were chosen and the pumps were operated at 800 °C.

In the case of $SrCe_{0.95}Yb_{0.05}O_{3-\alpha}$, the evolution rate of hydrogen at the cathode well agrees with Faraday's law up to around 600 mA/cm^2 as shown in Fig. 3(a) (the reduction in Faradaic efficiency at higher current densities is discussed in Section 4.3). In addition, overpotentials due to the electrode reactions are fairly low as seen in Fig. 3(b). Hydrogen has the chemical energy of 1.35 V to form water in voltage scale (enthalpy change of water formation divided by $2F$; F being Faraday's constant), so that the energy loss (reaction overpotentials) of a few hundred mV is not a high value from a view point of hydrogen separation.

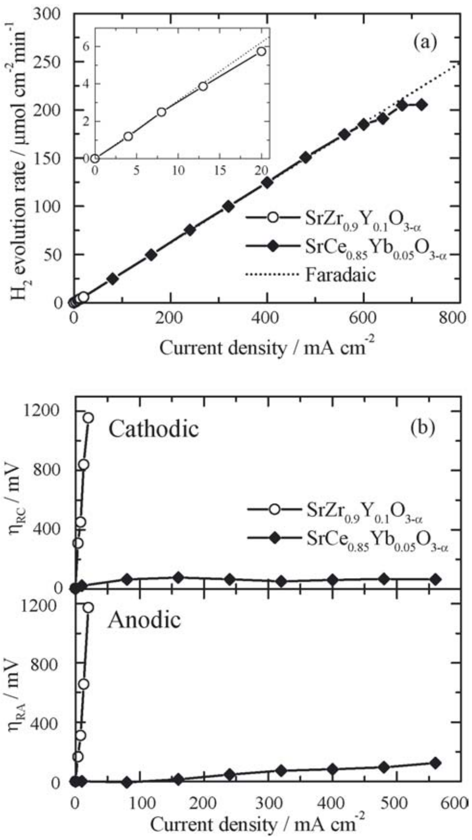

Fig. 3. (a) Evolution rate of hydrogen at the cathode and (b) electrode overpotentials in the ionic current region during hydrogen pumping at 800 °C as functions of current density using $SrZr_{0.9}Y_{0.1}O_{3-\alpha}$ and $SrCe_{0.95}Yb_{0.05}O_{3-\alpha}$ electrolytes; the dotted line in (a) indicates the theoretical evolution rate of hydrogen calculated from Faraday's law. The left upper graph in (a) is shown in smaller scale for $SrZr_{0.9}Y_{0.1}O_{3-\alpha}$ and concentration polarizations were excluded in (b). Porous platinum electrodes were used; anode gas = moist H_2 ($p_w = 2.3 \times 10^3$ Pa, fed at 30 mL min^{-1}); cathode gas = moist Ar ($p_w = 2.3 \times 10^3$ Pa, fed at 30 mL min^{-1}).

In contrast, the hydrogen pump using $SrZr_{0.9}Y_{0.1}O_{3-\alpha}$ has quite poor performance. As shown in Fig. 3(a) the hydrogen-pumping rate deviates from the Faradaic one at a current density as low as 20 mA/cm^2. Fig. 3(b) indicates quite high overpotentials (>1 V) both at the anode and cathode needed for such a low current density. Therefore, the hydrogen pump using $SrCe_{0.95}Yb_{0.05}O_{3-\alpha}$ electrolyte is much superior in the performance of both energy efficiency and hydrogen-pumping rate.

The above experimental results suggest that the electrocatalytic activity of Pt for the cerate will be much higher than that for the zirconate, and thus is responsible for the difference in their hydrogen-pumping performance. We usually assume a triple phase boundary of gas/electrode/electrolyte as a place where electrode reactions take place. Actually, the electrode reaction zone will not be restricted to the triple phase boundary, which is mathematically one dimensional, but should spread to the gas/electrode interface by surface diffusion of ionic species on the electrode and/or to the gas/electrolyte interface by an electronic species locally present in the electrolyte. If one assumes the similar microstructure of porous Pt electrodes for the two cases, the latter gas/electrolyte interface might be a reason for the large difference in the electrode overpotentials between the combinations of Pt/$SrCe_{0.95}Yb_{0.05}O_{3-\alpha}$ and Pt/$SrZr_{0.9}Y_{0.1}O_{3-\alpha}$. How the interfaces differ with the kind of electrolyte is not clear. It should be investigated further how the defect equilibriums differ in the electrolyte facing the metal electrode from those in the bulk property.

4.3. Reduction in current efficiency

Hydrogen-pumping rate with $SrCe_{0.95}Yb_{0.05}O_{3-\alpha}$ shown in Fig. 3(a) deviates lower than the Faradaic rate at a current density higher than 600 mA/cm^2. For this phenomenon, the partial oxide ionic conduction in the oxide electrolyte, explained in the former section, will be responsible [18,19]. By the oxide ionic charge carrier, the following electrode reactions can be assumed:

$$H_2O + 2e^- \rightarrow H_2 + O^{2-} \text{ (cathode)} \quad (10)$$

$$H_2 + O^{2-} \rightarrow H_2O + 2e^- \text{ (anode)} \quad (11)$$

Water vapor is decomposed to form hydrogen and oxide ion at the cathode. These reactions have the same number of electrons (two electrons) per molecular hydrogen as the electrode reactions in Eqs. (5) and (6) have, so that the Faraday's law for the evolution of hydrogen will still be maintained. These reactions due to the oxide ionic charge carriers consume water vapor at the cathode; from the change in water vapor pressure at the cathode outlet, the oxide-ionic transport number was estimated to be 0.1 (the rest 0.9 is attributable to the protonic transport number) [18,19]. The decrease in the current efficiency from unity occurs on the exhaustion of water at the cathode. Therefore, the water vapor at the cathode has a role in avoiding too reducing an atmosphere which can cause the electronic conduction in the electrolyte. By supplying sufficient water vapor to the cathode compartment, the pumping current density higher than 1 A/cm^2 is achievable [19].

4.4. Chemical stability

As explained above, $SrCe_{0.95}Yb_{0.05}O_{3-\alpha}$ electrolyte has excellent applicability in hydrogen pumps. However, the electrolyte is reactive with CO_2, so that the electrolyte can be used only under the condition that CO_2 can be excluded. Fig. 4 shows the XRD patterns of $SrCe_{0.95}Yb_{0.05}O_{3-\alpha}$ and $SrZr_{0.9}Y_{0.1}O_{3-\alpha}$ as prepared and after being exposed in 100% CO_2 at 800 °C for 3 h. After the CO_2 treatment, $SrCe_{0.95}Yb_{0.05}O_{3-\alpha}$ obviously reacted with CO_2 by the reaction in Eq. (12) to decompose into $SrCO_3$ and CeO_2.

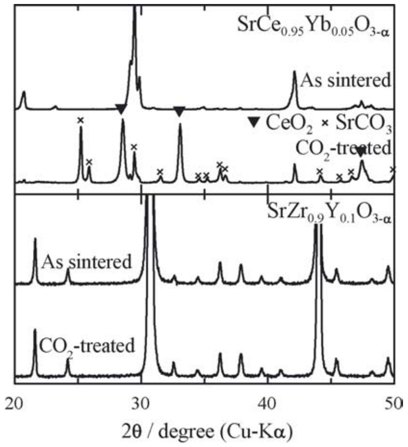

Fig. 4. XRD patterns of $SrCe_{0.95}Yb_{0.05}O_{3-\alpha}$ (upper) and $SrZr_{0.9}Y_{0.1}O_{3-\alpha}$ (lower) as prepared and after treated in CO_2 at 800 °C for 3 h. Peaks indicated by (▼)and (×) are assigned to CeO_2 and $SrCO_3$, respectively.

$$SrCeO_3 + CO_2 \rightarrow SrCO_3 + CeO_2 \quad (12)$$

From thermodynamic data [20], this reaction has a negative free energy change below 1050 °C at the unique activity of CO_2. In the case of $SrZr_{0.9}Y_{0.1}O_{3-\alpha}$, the XRD patters have no changes after the CO_2 treatment. If we aim to separate hydrogen from the reformed gases of hydrocarbons, which is the most demanded kind of hydrogen separation for mass production of hydrogen, CO_2 will inevitably generate in the H_2–CO mixture due to the reaction equilibrium in Eq. (13).

$$CO + H_2O \rightleftarrows CO_2 + H_2 \quad (13)$$

This equilibrium is even at around 800 °C [20]. $SrCe_{0.95}Yb_{0.05}O_{3-\alpha}$ electrolyte is reactive with CO_2 at its working temperature, e.g., 800 °C, and thus the electrolyte is not adequate for hydrogen separation from the reformed gases. Zirconate-based electrolyte is only available for this purpose. Several studies suggest that cerate–zirconate solid solutions have durability to CO_2 [21–23]. In our preliminary experiments, however, the partial substitution of Zr will also reduce the catalytic activity of Pt electrodes and is not hopeful solution. We are investigating the improvement of electrode performance for zirconate-based electrolytes and some candidate electrodes have been found; the results will be presented elsewhere (to be submitted).

5. Hydrogen permeation membrane

5.1. Protonic–electronic mixed conductors

The hydrogen pumps described in the former section employ the HTPCs as proton-conducting electrolytes that have negligibly low electronic conductivity under operation. Conversely, if we can add electronic conductivity in the proton-

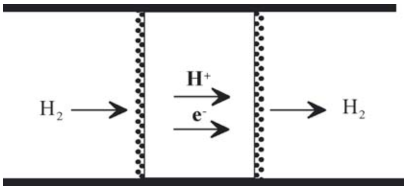

Fig. 5. Hydrogen permeation via protonic–electronic mixed-conducting membrane.

conducting solids, hydrogen permeation will occur through the materials; such mixed conductors may not usually be counted as HTPCs since the term is referred to electrolytes, i.e., the dominant ionic conductors. The schematic principle of the hydrogen-permeating membrane is presented in Fig. 5. No external electric power supply is necessary, so that the electrodes and external electrical circuit are excluded and a simple hydrogen separator can be constructed [24]; the membrane uses the hydrogen potential gradient as the driving force for the hydrogen transport.

It seems there have been no accepted materials so far as the protonic–electronic mixed conductors that allow high hydrogen drain. Therefore, in contrast to the conventional HTPCs that already have long history, the protonic–electronic mixed conductors are not established but in quest now. We report here the protonic–electronic mixed conduction occurring in ruthenium-doped perovskites, $BaCe_{0.9-x}Y_{0.1}Ru_xO_{3-\alpha}$ ($x = 0$–0.1) [25].

5.2. Theoretical backgrounds and experimental procedures

The hydrogen permeation through the specimens was examined at 800 °C using the following cell:

$$H_2 \text{ at } p(H_2,\ \text{supp}),\ \text{Pt}|\text{specimen}|\text{Pt},\ \text{Ar}. \tag{14}$$

If one assumes proton (H^+), oxide ion (O^{2-}), conduction electron (e) and electron hole (h) as ionic and electronic charge carriers, hydrogen evolution at the permeating side will obey the ambipolar diffusion mechanism, expressed by Eq. (15) [25].

$$J_{H2} \approx \frac{RT}{4F^2L}\frac{(\sigma_{H^+}+\sigma_{O^{2-}})(\sigma_e+\sigma_h)}{\sigma_T}\ln\frac{p(H_2,\text{supp})}{p(H_2,\text{perm})} \tag{15}$$

in which σ_j and σ_T are the partial conductivity of j species and the total conductivity, respectively, and L is the thickness of the mixed conductor; the equation assumes the equal water vapor pressure in the two compartments and constant partial conductivities. The ambipolar hydrogen flux is proportional to $\ln(p(H_2,\text{supp})/p(H_2,\text{perm}))$. The test cell construction was the same as that used for the hydrogen concentration cell measurements. H_2/Ar mixtures were fed to the left compartment of cell (14) and argon gas was passed to sweep the hydrogen evolved in the right compartment. The gases contained water vapor at 1.9×10^3 Pa and were fed at 30 mL/min. The partial pressures of hydrogen in the Ar sweep gas, $p(H_2, \text{perm})$ was determined by gas chromatography.

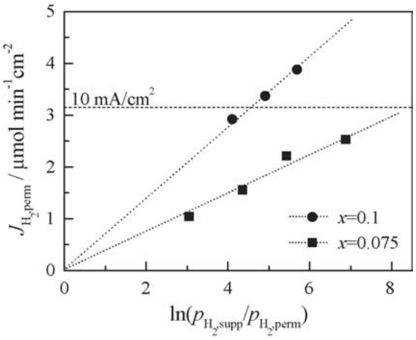

Fig. 6. Hydrogen permeation flux of $BaCe_{0.9-x}Y_{0.1}Ru_xO_{3-\alpha}$ ($x = 0.05$, 0.075) at 800 °C as a function of the logarithm of the ratio of hydrogen partial pressure at the hydrogen-supplying side, $p(H_2, \text{supp})$, to that at the permeating side, $p(H_2, \text{perm})$.

X-ray absorption spectroscopy (XAS) [26,27] was employed to estimate the electronic charge carrier. Since this technique elucidates unoccupied density of states of electron holes, unoccupied states in the valence band, can be detected. The measurements were conducted at the revolver undulator beamline BL-19B at the Photon Factory of the High Energy Accelerator Organization, Tsukuba, Japan. Synchrotron radiation was monochromatized using a varied-line spacing plain grating. The XAS spectra were measured using a Si photodiode. The samples were scraped in situ with a diamond file in vacuum to obtain a clean surface. Prior to the measurements, the specimen were either as sintered in air or annealed in moist 1% H_2 at 800 °C for 10 h to compare the electronic structure in the oxidative and reducing atmospheres.

5.3. Hydrogen permeability

Fig. 6 shows the hydrogen flux through $BaCe_{0.9-x}Y_{0.1}Ru_xO_{3-\alpha}$ ($x = 0.075$, 0.1) at 800 °C measured with the cell in Eq. (14); hydrogen permeation was not experimentally observed for the Ru-undoped sample ($x = 0$). It is notable that the hydrogen flux is proportional to $\ln(p(H_2, \text{supp})/p(H_2, \text{perm}))$, suggesting that the hydrogen transport occurred in accordance with the ambipolar diffusion mechanism in Eq. (15). It is evident that the hydrogen permeation occurs via the ionic-electronic mixed conduction in the Ru-doped perovskites. The maximum hydrogen flux obtained is 6.5×10^{-8} mol/s cm^2 ($x = 0.1$), equivalent to the internally short-circuited current density of 12.5 mA/cm^2.

As explained in previous sections, protonic and oxide-ionic change carriers can be assumed. By observing the change in water vapor pressure in the permeating compartment, a half of the ionic conduction was estimated to be due to the oxide ions and the other half could be attributed to protons in the case of $BaCe_{0.8}Y_{0.1}Ru_{0.1}O_{3-\alpha}$ at 800 °C. This fraction is quite similar to that of the base HTPC of the ac-

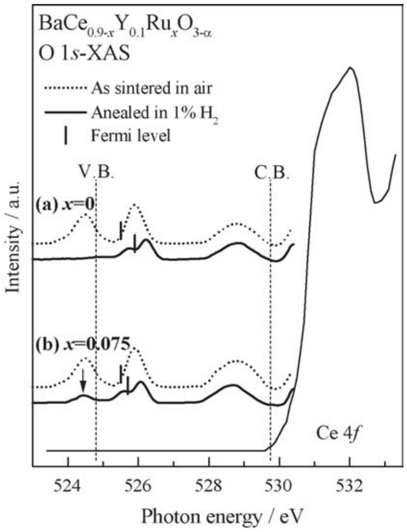

Fig. 7. XAS spectra of $BaCe_{0.9-x}Y_{0.1}Ru_xO_{3-\alpha}$ ($x = 0$, 0.075); spectra overviews and 10 times magnified spectra around the band gap regions are shown. The enlarged spectra in dashed lines are of the specimens as sintered in air and those in solid lines are of the specimens after annealed in moist 1% H_2 at 800 °C for 10 h.

ceptor doped barium cerate [11,12]. Therefore, the doping of Ru will provide an electronic conduction without changing the protonic/oxide-ionic fraction of conductivity in the acceptor doped $BaCeO_3$.

5.4. Mixed conduction mechanism

In order to estimate if electron holes or conduction electrons are responsible for the electronic conduction, soft X-ray absorption spectroscopy (XAS) was employed, expecting that the electron hole can be observed by this technique [26,27]. Fig. 7 shows the XAS spectra of $BaCe_{0.9-x}Y_{0.1}Ru_xO_{3-\alpha}$ ($x = 0$ and 0.075) as sintered in air and after annealed in moist 1% H_2 at 800 °C for 10 h. In case that the specimens were untreated after sintering in ambient air containing humidity, the spectra of both Ru-undoped and Ru-doped specimen have peaks just below the top of the valence band. The peaks at this position are attributable to electron hole present by the defect equilibrium shown in Eq. (1). The Ru-undoped specimen annealed in moist 1% H_2 has no peak at the position, due to the equilibrium leaning to the left as $p(O_2)$ decreases. However, in the case of the Ru-doped sample, the hole peak remains even after the treatment in the reducing atmosphere. This fact suggests that the electronic species for the mixed conduction will be attributed to the hole formed in the Ru-doped materials.

It is not clarified how the Ru doping results in the formation of electron hole in the reducing atmosphere. But, it is possible to assume a kind of energy level produced by the Ru-4*d* orbitals, which locate just above the valence band and accept electrons from the valence band to generate electron holes. Additional experiments, e.g., determination of the valence of Ru and the conductivity dependences on $p(O_2)$ and $p(H_2O)$, will provide a definite model for the protonic–electronic mixed conduction in the Ru-doped perovskites.

The hydrogen permeability of the materials is still low compared to the conventional methods. For example, Pd–Ag membranes have 10–100 times higher permeability in very rough estimation; the difference in the mechanisms (driving forces) of hydrogen diffusion is neglected. However, this report provides the possible mechanism for the mixed-protonic–electronic conduction and will lead to the next finding of new materials.

Acknowledgements

This study was supported by CREST of Japan Science and Technology (JST), Industrial Technology Research Grant Program in 02B65001c from New Energy and Industrial Technology Development Organization (NEDO) of Japan and a 21st Century COE Program Grant of the International COE of Flow Dynamics from the Ministry of Education, Culture, Sports, Science and Technology.

References

[1] H. Iwahara, T. Esaka, H. Uchida, N. Maeda, Solid State Ionics 3–4 (1981) 359.
[2] H. Iwahara, H. Uchida, N. Maeda, Solid State Ionics 11 (1983) 109.
[3] H. Uchida, H. Yoshikawa, H. Iwahara, Solid State Ionics 34 (1989) 103.
[4] T. Scherban, A.S. Nowick, Solid State Ionics 35 (1989) 189.
[5] T. Yajima, H. Iwahara, Solid State Ionics 50 (1992) 281.
[6] T. Yajima, H. Iwahara, Solid State Ionics 53–56 (1992) 983.
[7] N. Bonanos, M. Mogensen, Solid State Ionics 97 (1997) 483.
[8] H. Iwahara, H. Uchida, K. Ogaki, K. Ono, J. Electrochem. Soc. 135 (1988) 529.
[9] N. Bonanos, B. Ellis, K.S. Knight, M.N. Mahamood, Solid State Ionics 35 (1989) 179.
[10] H. Iwahara, H. Uchida, K. Morimoto, J. Electrochem. Soc. 137 (1990) 462.
[11] H. Iwahara, T. Yajima, T. Hibino, H. Ushida, J. Electrochem. Soc. 140 (1993) 1687.
[12] H. Iwahara, T. Yajima, H. Ushida, Solid State Ionics 70–71 (1994) 267.
[13] Ma Guilin, T. Shimura, H. Iwahara, Solid State Ionics 110 (1998) 103.
[14] H. Iwahara, T. Yajima, T. Hibino, K. Ozaki, H. Suzuki, Solid State Ionics 61 (1993) 65.
[15] K.D. Kreuer, Solid State Ionics 125 (1999) 285.
[16] H. Iwhara, Solid State Ionics 125 (1999) 271.
[17] T. Schober, Solid State Ionics 162–163 (2001) 277.
[18] H. Matsumoto, S. Hamajima, T. Yajima, H. Iwahara, J. Electrochem. Soc. 148 (2001) D121.
[19] H. Matsumoto, S. Hamajima, H. Iwahara, Solid State Ionics 145 (2001) 25.
[20] M.W. Chase Jr., J. Phys. Chem. Ref. Data Monograph 9—NIST-JANAF Thermochemical Tables, fourth ed., 1998.
[21] T. Matzke, M. Cappadonia, Solid State Ionics 86–88 (1996) 659.

[22] S. Wienströer, H.-D. Wiemhöfer, Solid State Ionics 101–103 (1997) 1113.
[23] K.H. Ryu, S.M. Haile, Solid State Ionics 125 (1999) 355.
[24] T. Norby, Y. Larring, Solid State Ionics 136–137 (2000) 139.
[25] H. Matsumoto, T. Shimura, T. Higuchi, H. Tanaka, K. Katahira, T. Otake, T. Kudo, K. Yashiro, A. Kaimai, T. Kawada, J. Mizusaki, J. Electrochem. Soc., in press.
[26] T. Higuchi, T. Tsukamoto, K. Kobayashi, S. Yamaguchi, Y. Ishiwata, N. Sata, K. Hiramoto, M. Ishigame, S. Shin, Phys. Rev. B 65 (2002) 033201.
[27] T. Higuchi, T. Tsukamoto, N. Sata, M. Ishigame, K. Kobayashi, S. Yamaguchi, S. Shin, Solid State Ionics 154–155 (2002) 735.